CELLULAR NEUROSCIENCE

Uncontrolled mitochondrial calcium uptake underlies the pathogenesis of neurodegeneration in MICU1-deficient mice and patients

Raghavendra Singh[1]†, Adam Bartok[1,2]†, Melanie Paillard[1], Ashley Tyburski[3], Melanie Elliott[3], György Hajnóczky[1]*

Dysregulation of mitochondrial Ca^{2+} homeostasis has been linked to neurodegenerative diseases. Mitochondrial Ca^{2+} uptake is mediated via the calcium uniporter complex that is primarily regulated by MICU1, a Ca^{2+}-sensing gatekeeper. Recently, human patients with MICU1 loss-of-function mutations were diagnosed with neuromuscular and cognitive impairments. While studies in patient-derived cells revealed altered mitochondrial calcium signaling, the neuronal pathogenesis was difficult to study. To fill this void, we created a neuron-specific MICU1-KO mouse model. These animals show progressive, abnormal motor and cognitive phenotypes likely caused by the degeneration of motor neurons in the spinal cord and the cortex. We found increased susceptibility to mitochondrial Ca^{2+} overload-induced excitotoxic insults and cell death in MICU1-KO neurons and MICU1-deficient patient-derived cells, which can be blunted by inhibiting the mitochondrial permeability transition pore. Thus, our study identifies altered neuronal mitochondrial Ca^{2+} homeostasis as causative in the clinical symptoms of MICU1-deficient patients and highlights potential therapeutic targets.

INTRODUCTION

Mitochondrial metabolism, redox, and Ca^{2+} homeostasis are central to orchestrating neuronal function in health (*1*), and their impairments are linked to neurodegenerative diseases (amyotrophic lateral sclerosis, Alzheimer's disease, Parkinson's disease, and Huntington's disease) (*2*–*11*). In the past years, numerous patients with neuromuscular and cognitive impairments have been identified with the loss-of-function mutation of MICU1 (*12*–*16*), the Ca^{2+} sensing regulator of the mitochondrial calcium uniporter complex (mtCU), which is the main pathway for mitochondrial Ca^{2+} entry (*17*–*20*). These studies suggest a direct link between the patients' symptoms and the altered mitochondrial calcium signaling, which might be also relevant for the common neurodegenerative diseases; however, thus far, no evaluation in a neuronal model has been performed.

Neurons developed complex Ca^{2+} signaling pathways that are engaged in the control of cellular metabolism, cell survival, gene expression, and membrane excitability. To induce a cytoplasmic $[Ca^{2+}]$ ($[Ca^{2+}]_c$) rise, Ca^{2+} enters neurons mainly through voltage-gated or ligand-activated Ca^{2+} channels (*21*), and mobilized from the endoplasmic reticulum Ca^{2+} store (*22*). Mitochondria take up Ca^{2+} during the $[Ca^{2+}]_c$ signals and subsequently release Ca^{2+} back to the cytoplasm. Although only a relatively small fraction of Ca^{2+} are handled by mitochondria during physiological $[Ca^{2+}]_c$ signals, because of their strategic positioning, mitochondrial Ca^{2+} influx and efflux play a role in the spatiotemporal organization of the $[Ca^{2+}]_c$ signals (*1*). Mitochondrial Ca^{2+} uptake also results in a rise in mitochondrial matrix $[Ca^{2+}]$ ($[Ca^{2+}]_m$) that stimulates oxidative ATP production and other intramitochondrial targets (*23*). Thus, neurons need a powerful mitochondrial Ca^{2+} transport mechanism under tight control.

Ca^{2+} is accumulated in the mitochondria via a Ca^{2+}-selective ion channel, mtCU, located in the inner mitochondrial membrane. mtCU is a hetero-oligomeric channel complex composed of the pore-forming protein, MCU (*24*, *25*); an essential scaffold, essential MCU regulator (EMRE) (*26*); and Ca^{2+}-sensitive regulators, MICU1 (*27*), MICU2 (*28*), and MICU3 (*29*). Loss of MCU or EMRE prevents mitochondrial Ca^{2+} uptake. In addition to supporting pore formation by tetrameric MCU, EMRE anchors MICU1 to MCU (*30*). However, MICU1 also binds directly to the DIME motif of the MCU tetramer (*31*). On the basis of recent structural data, the mtCU complex has 4:4:1:1 stoichiometry of MCU, EMRE, MICU1, and MICU2 (*32*). A dimer of MICU proteins appears to determine both the threshold and cooperative activation of the mtCU by Ca^{2+}, thus providing a mechanism for the supralinear $[Ca^{2+}]_c$ activation of the mtCU (*20*, *33*). The MICU proteins have EF-hand Ca^{2+}-binding domains (*32*, *33*) localized to the intermembrane space (*20*, *34*), making them suitable to sense $[Ca^{2+}]_c$ signals for the control of mitochondrial Ca^{2+} uptake. In practical terms, Ca^{2+}-free MICUs support closure of the mtCU pore and suppresses mitochondrial Ca^{2+} uptake, whereas the Ca^{2+}-bound MICUs promote the Ca^{2+} flux. Because MICU2 has lower and MICU3 has higher affinity for Ca^{2+} than MICU1, the MICU1-MICU2 dimer elevates, whereas the MICU1-MICU3 dimer lowers the $[Ca^{2+}]_c$ threshold for mtCU opening (*29*, *33*, *35*). Evidence supports that MICU1 and MICU2 are broadly expressed (*28*, *36*), whereas MICU3 is mostly expressed in the brain (*34*), but the effect of age or neurodegeneration on their abundance remains elusive.

Ca^{2+} uptake is balanced by Ca^{2+} efflux mediated by Ca^{2+} exchangers, like NCLX, an Na^+-dependent exchanger with relevance in the brain (*37*, *38*), and by a large conductance channel, the permeability transition pore (PTP), that commonly opens under mitochondrial Ca^{2+} overload conditions, including excitotoxic injury in neurons (*39*).

Loss of MCU in mice does not cause neurological defects but causes skeletal muscle (SM) dysfunction during strenuous work (*40*). We have shown that lack of MICU1 in SM alters the cellular

---

[1] MitoCare Center, Department of Pathology, Anatomy and Cell Biology, Thomas Jefferson University, Philadelphia, PA, USA. [2] Depertment of Biochemistry, Semmelweis University, Budapest, Hungary. [3] Department of Neurological Surgery, Thomas Jefferson University, Philadelphia, PA, USA.
*Corresponding author. Email: gyorgy.hajnoczky@jefferson.edu
†These authors contributed equally to this work.

Ca^{2+} homeostasis during myofiber contraction and leads to muscle atrophy, SM weakness, fatigue, and weakened repair of the damaged sarcolemma (*41*). However, the role of MICU1 regulation of mtCU Ca^{2+} uptake in the development of neuronal phenotype like learning disability and motor dysfunction is still enigmatic. Here, we introduce a novel neuronal MICU1–knockout (KO) mouse (nKO) model to study the role of the mtCU gating by Ca^{2+} in neuronal biology and in the neurological impairments of patients. The nKO shows progressive, abnormal motoric and cognitive phenotype and degeneration of motor neurons in the spinal cord and the cortex. We found lower Ca^{2+} uptake threshold and maximal capacity in isolated cortical mitochondria increased susceptibility to mitochondrial Ca^{2+} overload and cell death in primary, cultured KO neurons, similarly to fibroblasts and lymphoblast of a human MICU1-deficient patient. Our study identifies the common causative of the clinical symptoms of the MICU1-deficient patients and the phenotype of the MICU1-KO mice at the level of neuronal mitochondrial Ca^{2+} homeostasis.

RESULTS

Eno2-Cre knocked down MICU1 after birth

To establish a neuron-specific MICU1-KO (nKO) mouse model, we used MICU1-floxed mice (*42*) and the Eno2-Cre-loxP system (*43*, *44*) to target exon 3 of the MICU1 gene in neurons. nKO animals bred and developed normally, with no signs of impairments in the colony. Littermate MICU1-floxed [wild-type (WT)] animals were housed together with nKO animals and used as control in the experiments. To validate the KO of MICU1, we isolated mitochondria from the brain cortex in different age groups and immunoblotted for proteins involved in mitochondrial Ca^{2+} homeostasis (Fig. 1, A and B, and fig. S1A). From as early as 3 weeks of age, MICU1 protein was significantly decreased in nKO animals, although a remaining amount, likely derived from glial mitochondria in the prepared sample (*45*), was present in nKO animals. Decrease in MICU1 abundance was associated with reduced MICU3 and EMRE protein levels in all postnatal age groups, and in MICU2 and MCU at 9 to 12 months of age. EMRE decrease, a possible adaptive mechanism, has been also

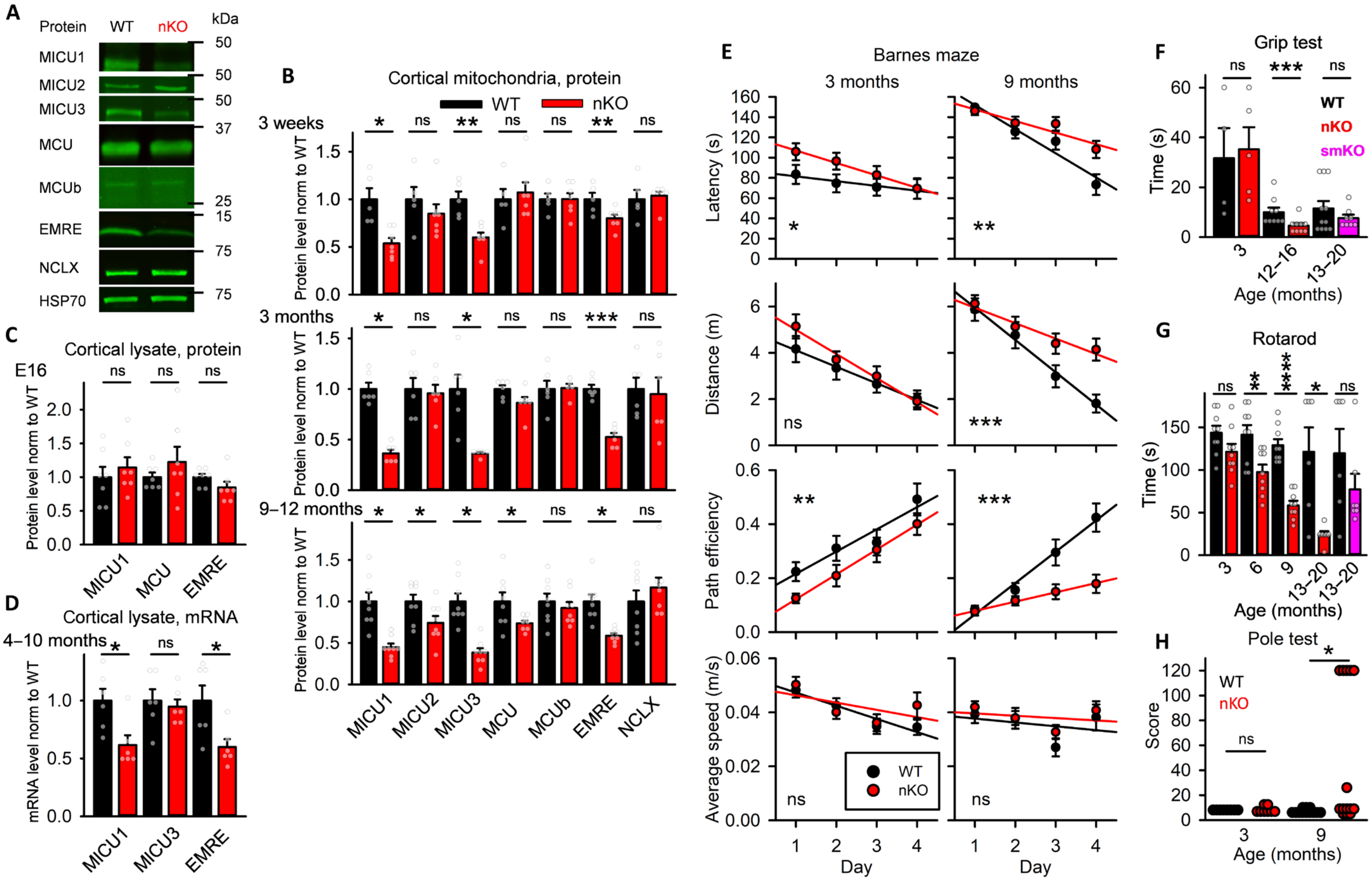

Fig. 1. Progressive cognitive and motor impairments in neuronal MICU1-KO mice. (**A**) Immunoblot image of proteins involved in mitochondrial Ca^{2+} homeostasis in isolated cortical mitochondria of 3-month-old mice. HSP70 was used as loading control. (**B**) Protein levels relative to HSP70, normalized to those in WT, in cortical mitochondria from different age groups ($N = 5$ to 8 animals per condition). (**C**) Protein levels in embryonic cortical lysates ($N = 7$ pairs). (**D**) mRNA levels in the cortex determined with qPCR on cDNA transcript of isolated mRNA and normalized to the levels measured in WT ($N = 6$ pairs). (**E**) Three- and 9-month-old animals tested on Barnes maze. Latency [depicts the time (seconds) taken by animals to find the escape box), distance (total distance traveled between the starting point and the escape box during the trial), path efficiency (0-1, where 1 is a straight line between the starting point and the escape box), and average speed are shown, three trials on four consecutive testing days ($N = 8$ to 9 pairs each age]. (**F**) Grip strength measured with wire-hanging test. Latencies to fall in different age groups of nKO and smKO mice ($N = 4$ to 9 animals per group). (**G**) Rotarod test applying linear acceleration. Maximal duration times before falling in different age groups of nKO and smKO mice ($N = 4$ to 9 animals per group). (**H**) Scores on the pole test in 3- and 9-month-old animals ($N = 8$ to 14 animals per group). (E to H) In each age group, naïve animals were tested. ns, not significant; $P > 0.05$; $*P < 0.05$; $**P < 0.01$; $***P < 0.001$.

observed in other model systems (*41*, *42*, *46*). By contrast, in embryonic day 16 (E16; 16th day of gestation) cortical lysates, we found no changes in the levels of MICU1, MCU, or EMRE proteins (Fig. 1C and fig. S1A). This is consistent with the expression of Cre initiating after birth and thus the presence of MICU1 during embryonic development, which likely explains the viability of the colony as opposed to the whole-body MICU1-KO (KO) (*42*). In terms of gene expression in the brain cortex of adult nKO animals, we found decreased mRNA levels of MICU1 and EMRE, but not of MICU3 (Fig. 1D). To test whether any perturbations of the mtCU complex subunits occurred beyond the nervous system in the nKO mice, we performed immunoblots of mitochondria isolated from the SM. No difference among the age-matched (15 to 18 months) nKO and WT animals was detected (Fig. 1B). This suggests that Eno2-Cre–mediated MICU1-KO is specific to neurons.

Progressive demise in learning and motor ability in nKO mice

Having a viable nKO mouse model gave us an opportunity to explore the effect of neuronal loss of MICU1 on cognitive and motor behavior of animals. To start probing cognitive impairments, spatial learning was tested with a Barnes maze (*47*) in young (3 months, male) and older (9 months, male) animals (Fig. 1E). At 3 months of age, only minor differences were observed for all parameters tested between WT and nKO animals during the four trial days. Differently, at 9 months, latency to find the target/scape box and distance traveled were greatly increased in the nKO, suggesting that the learning ability of the nKO lagged behind that of the WT animals. The average speed, a measure of the basic locomotor functions, did not show differences at any age between nKO and WT animals. We next studied the motor behavior of animals from different ages groups (3, 9, and 12 to 20 months). The grip test (Fig. 1F) and the rotarod test (Fig. 1G) (*48*) both showed age-dependent, progressive decreases in performance for nKO animals. In comparison, SM-specific MICU1-KO (smKO) (*41*) animals did not show a significant decrease in performance in the grip and rotarod tests (Fig. 1, F and G). With the pole test, we did not find any significant difference at the age of 3 months, in contrast, although at 9 months, we observed that ~30% of the MICU1-nKO could not perform the task (Fig. 1H). Notably, the above-described pole, grip, and rotarod results were obtained with male mice, but we also performed similar studies on a small cohort of female mice, in which the nKO showed a clear trend in all tests to a similar phenotype to what we observed in male animals (fig. S1C). Body weight and muscle fiber morphology did not indicate SM atrophy in nKO animals that might be due to unaltered MICU1 protein levels in SM (fig. S1, B and D). Thus, our results link neuronal MICU1 to both learning and motor functions and support neuron-specific MICU1 loss as the dominant factor in the progressive motor dysfunction in patients with MICU1 mutations. Moreover, the progressive behavioral defects due to MICU1 absence, as in human patients, affect both genders in nKO mice.

Spinal cord motoneuron loss and cortical dendritic spine morphology alterations in nKO mice

Because a set of behavioral tests (grip test, rotarod, and pole test) performed on adult male and female nKO animals (fig. S1B) show a similar trend in all tests points, we randomly chose males to carry out further experiments. To understand the pathological basis of the motor disabilities in nKO animals, we examined the motor neurons in the spinal cord anterior horn in aged animals (15 to 19 months, Nissl staining). We found reduced Nissl-positive neuronal counts and a high percentage of the neurons with vacuolization in the nKO animals (Fig. 2A). Motor neuron-specific staining [choline acetyltransferase (ChAT)] confirmed decreased motor neuron counts (Fig. 2B), which were coupled with overexpression of glial fibrillary acidic protein (GFAP), a marker of reactive gliosis in the spinal cord of nKO animals (Fig. 2C), confirming lower motor neuron degeneration (*49*, *50*) in the absence of MICU1.

Mitochondrial requirement in dendritic spine morphogenesis (*51*) and spine pathology in motor (*52*) and cognitive dysfunction (*53*) led us to examine the barbarization of neuronal dendrites in the prefrontal cortex of animals in different age groups (3, 9, and 18 to 19 months) (Fig. 2, D to G). We found abnormal dendritic spines characterized by decreased number, shorter length, and smaller head area and diameter in nKO animals that progressed with age (Fig. 2F). Although some of the abnormal phenotypes (head area and diameter) are already present at 3 months, we could not observe significant differences with detailed morphological analysis of the dendritic spines (Fig. 2G). However, in aged animals (18 to 19 months), we found higher proportion of premature (thin or filopodia) and lower proportion of mature (mushroom) states in nKO animals (Fig. 2H), which further confirms the progressive nature of the neuronal phenotype. Degeneration of motor neurons in the spinal cord and altered dendritic arborization in the prefrontal cortex of nKO animals could be the cause of the motor defects.

To connect the in vivo animal and brain structure phenotype to Ca^{2+} homeostasis, first we isolated mitochondria from the cortex of aged nKO animals and evaluated their Ca^{2+} clearance. nKO brain mitochondria showed reduced Ca^{2+} uptake at high cytoplasmic $[Ca^{2+}]$ ($[Ca^{2+}]_c$), ~20 μM (Fig. 2, H and I), and increased use of total Ca^{2+} uptake capacity at submicromolar $[Ca^{2+}]_c$ (fig. S2, A to C) than age-matched WT. This replicates the previously described lower $[Ca^{2+}]_c$ threshold and decreased maximal Ca^{2+} flux in MICU1-deficient mitochondria (*20*, *33*, *46*, *54*).

Altered excitability and mitochondrial Ca^{2+} signaling in KO primary mouse neurons

Because in the nKO, MICU1 is knocked out only after birth, to further investigate the consequences of MICU1 loss in neuronal Ca^{2+} homeostasis, we used primary embryonic cortical neuronal cultures from the whole-body MICU1-KO (KO) mouse model (*42*). In the complete absence of MICU1 expression (Fig. 3, A and B), we found decreased abundance of MICU3 and EMRE proteins like in the 3-week-old or older nKO (Fig. 3A). In the embryonic neurons, MICU3 and EMRE both showed decreased mRNA levels (Fig. 3B).

We first stimulated the primary neurons with simultaneous addition of a γ-aminobutyric acid (GABA) receptor antagonist, Bicuculline (Bicu), and a K^+ channel inhibitor, 4-aminopyridine (4AP), to produce intracellular Ca^{2+} spiking via activation of the synaptic *N*-methyl-D-aspartate (NMDA) receptors (*55*–*57*). We measured $[Ca^{2+}]_c$ with fura2 and found that ~63% of MICU1-KO neurons did not display a $[Ca^{2+}]_c$ spike upon Bicu + 4AP exposure as compared with WT neurons where ~9% of neurons were nonresponsive (Fig. 3C). The difference in excitability might reflect altered synaptic activity in KO neurons. A recent study showed that the deletion of NCLX caused decreased synaptic activity and plasticity in neuronal mitochondria (*58*). When we included in our analysis only those neurons that were responsive to Bicu + 4AP, we found that $\Delta[Ca^{2+}]_c$ rise was not significantly attenuated in KO as compared with WT neurons

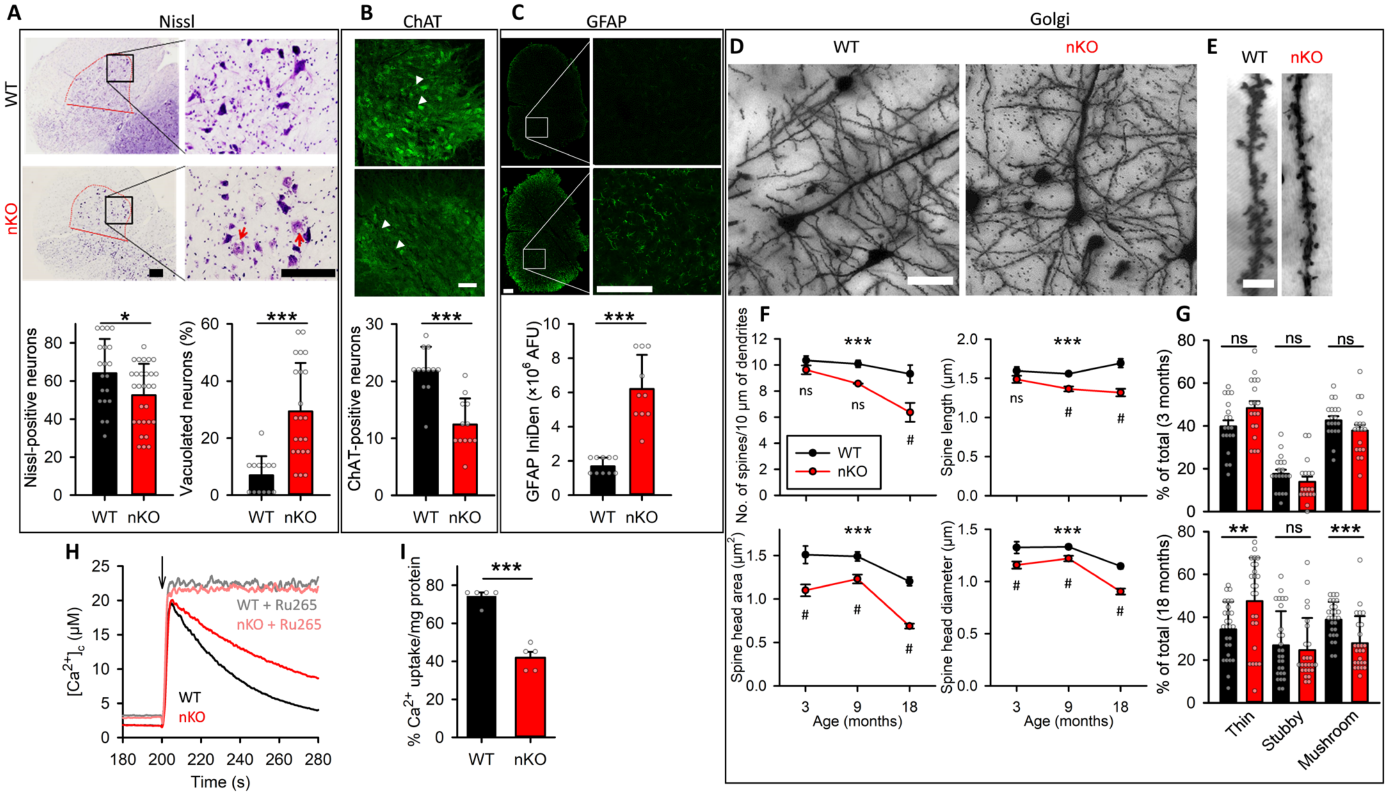

Fig. 2. Motor neuron degeneration in the spinal cord and altered dendritic spine morphology in the cortex of nKO mice. (**A**) Coronal sections of the spinal cord visualized by Nissl staining (scale bars, 200 μm). Neuron numbers determined in the anterior horn (red) (bottom left, $N = 20$ WT and 29 nKO sections from three WT and four nKO animals, 15 to 19 months). Neuronal morphology shown by the percentage of vacuolated cells (red arrows) (bottom right, $N = 13$ WT and 22 nKO slides). (**B**) Motor neurons visualized by immunofluorescent ChAT staining (top, white arrows; scale bar, 100 μm). Motor neuron numbers (bottom, $N = 12$ sections per condition). AFU, arbitrary fluorescence unit. (**C**) Gliosis shown by GFAP staining (top; scale bars, 200 μm) and measured as the mean fluorescence intensity (bottom, $N = 10$ sections from five animals per condition). (**D**) Pyramidal neurons in the prefrontal cortex in different age groups visualized by Golgi staining (samples from 18-month-old animals are shown; scale bar, 50 μm). (**E**) Dendritic spine morphology in 18-month-old WT and nKO animals (scale bar, 5 μm). (**F**) Dendritic spine density (top left), spine length (top right), spine head area (bottom left), and spine head diameter (bottom right) ($N = 3$ to 4 animals per group). (**G**) Classification of spine head morphology in 3-month-old (top) and 18-month-old (bottom) animals. (**H**) Clearance of a Ca^{2+} bolus (arrow, 50 μM $CaCl_2$), measured in cortical mitochondria in the presence or absence of Ru265 (5 μM). (**I**) Mitochondrial Ca^{2+} uptake per milligram of protein ($N = 5$ runs per condition, 12 to 15 months). ns, not significant; $P > 0.05$; $^*P < 0.05$; $^{**}P < 0.01$; $^{***}P < 0.001$.

(Fig. 3, D and E). As reported by others (*29*), the responsive cells showed $[Ca^{2+}]_c$ oscillation, without a change in the mitochondrial membrane potential ($\Delta\Psi_m$) measured by tetramethylrhodamine methyl ester (TMRM) (fig. S3, A to D).

To also study the mitochondrial Ca^{2+} homeostasis, we simultaneously measured $[Ca^{2+}]_c$ with fura2 and mitochondrial matrix $[Ca^{2+}]$ ($[Ca^{2+}]_m$) using a mitochondrial matrix–targeted calcium sensor, mito-GCaMP6f (Fig. 3, F and G). Difference images created by subtracting the prestimulation mito-GCaMP6f image from the ones obtained at 1 and 2 s of Bicu + 4AP stimulation showed an early rise in mito-GCaMP6f intensity in KO neurons (Fig. 3F). Similarly, the line graph also showed an early rise of $[Ca^{2+}]_m$ in the KO neurons (Fig. 3G, right). Furthermore, the delay of the half-maximal $[Ca^{2+}]_m$ signal relative to the half-maximal $[Ca^{2+}]_c$ rise was shorter in the KO as compared with WT (Fig. 3H).

Because the Bicu + 4AP–induced $[Ca^{2+}]_c$ oscillations are heterogeneous among the neurons, we next evoked action potentials using pulse field electric stimulation (PFES) to induce intracellular Ca^{2+} influx in the presence of NMDA (MK801) and AMPA (GYKI 52466) receptor inhibitors. Thus, we bypassed the neurotransmitter-dependent activation pathways and relied on voltage-gated ion channels to initiate neuronal Ca^{2+} responses. While the PFES-induced $[Ca^{2+}]_c$ rise was similar in both WT and KO neurons (Fig. 4A, left), the $[Ca^{2+}]_m$ rose earlier in KO neurons as compared with WT (Fig. 4, A, right, and B). The closer $[Ca^{2+}]_c$-$[Ca^{2+}]_m$ coupling during both Bicu + 4AP and electrical stimulations likely results from the absence of the gatekeeping function of MICU1 on MCU (*20*, *59*, *60*) in the KO neurons. To further test this, we quantified the resting $[Ca^{2+}]_m$ levels using a ratio metric genetic sensor, mtGEM-GECO, and observed higher resting $[Ca^{2+}]_m$ in MICU1-KO neurons as compared with WT (Fig. 4C). Along this line, discharging the basal mitochondrial calcium content by an uncoupler (FCCP and oligomycin) caused a greater $[Ca^{2+}]_c$ rise in KO than in WT neurons (Fig. 4, D and E), further supporting the lack of effective gatekeeping in MICU1-KO neurons.

Vulnerability to glutamate-induced delayed Ca^{2+} dysregulation and cell death in KO neurons

We have previously shown that MICU1-deficient mitochondria are prone to mitochondrial Ca^{2+} overload and cell death in cell lines and hepatocytes (*42*). Others have reported that overexpression of MCU leads to neuronal death (*61*). These findings led us to hypothesize

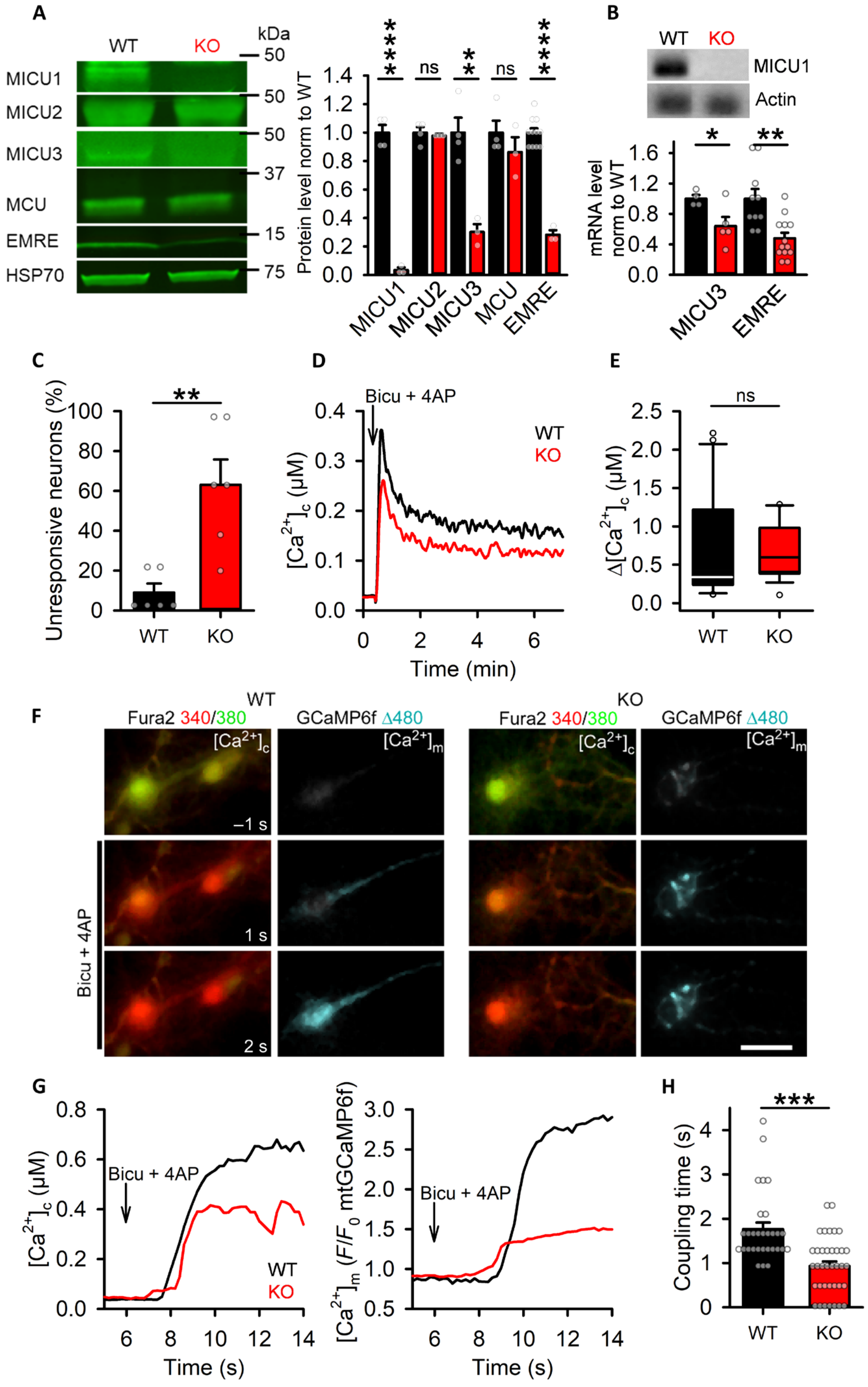

Fig. 3. Altered neuronal excitability and mitochondrial Ca^{2+} signaling in MICU1-KO neurons upon Bicuculline (Bicu) and 4-aminopyridine exposure (4AP). (**A**) Immunoblot images of proteins involved in mitochondrial Ca^{2+} uptake in WT and full-body MICU1-KO embryonic cortices (E16) (left). Protein levels relative to loading control HSP70 were normalized to those in WT (right, $N = 5$ WT and 3 KO). (**B**) mRNA levels determined with RT-PCR (top) and qPCR (bar graph) on cDNA transcript of embryonic cortical mRNA and normalized to the levels measured in WT ($N = 4$ to 13 per condition). (**C**) Percentage unresponsive neurons to Bicu (10 μM) and 4AP (100 μM) (Bicu + 4AP) (where $[Ca^{2+}]_c$ rise was not seen or seen >1 min after stimulation) (six independent experiments). (**D**) Mean $[Ca^{2+}]_c$ traces measured with fura2 upon Bicu + 4AP stimulation ($N = 26$ WT, 34 KO runs). (**E**) Bicu + 4AP–induced maximum $[Ca^{2+}]_c$ rise [calculated from the individual traces of (C)]. (**F**) Representative difference images (scale bar, 20 μm) of neurons showing $[Ca^{2+}]_c$ and $[Ca^{2+}]_m$ rise upon Bicu + 4AP stimulation. The images were created by subtracting mtGCaMP6f and fura2 image obtained at 1 and 2 s after Bicu + 4AP stimulation from the respective reference image acquired 1 s before stimulation. (**G**) Mean $[Ca^{2+}]_c$ (left) and $[Ca^{2+}]_m$ (right) traces in primary cortical neurons upon Bicu + 4AP stimulation. (**H**) Coupling time between $[Ca^{2+}]_c$ and $[Ca^{2+}]_m$ rise (calculated as time to $[Ca^{2+}]_m$ ½ max rise – time to $[Ca^{2+}]_c$ ½ max rise, $N = 30$ WT, 37 KO runs). ns, not significant; $P > 0.05$; $^{*}P < 0.05$; $^{**}P < 0.01$; $^{***}P < 0.001$; $^{****}P < 0.0001$.

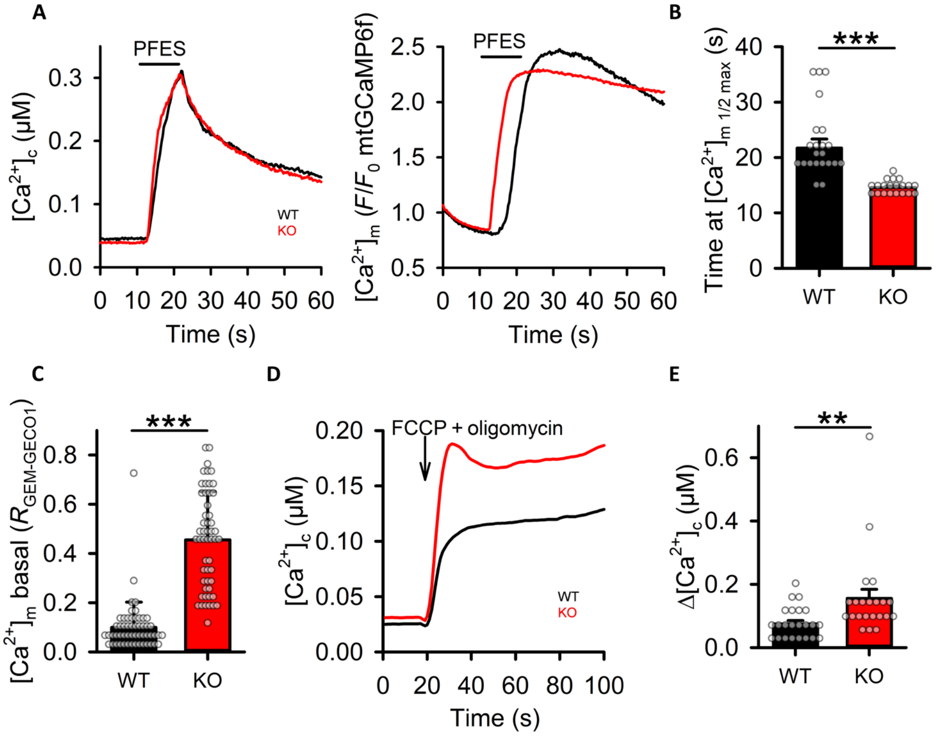

Fig. 4. Altered basal $[Ca^{2+}]_m$, and $[Ca^{2+}]_c$-$[Ca^{2+}]_m$ coupling upon PFES in MICU1-KO neurons. (**A**) Mean traces for $[Ca^{2+}]_c$ (left) and $[Ca^{2+}]_m$ (right) rise in primary cortical neurons upon 10 s of 20-Hz PFES ($N = 24$ WT and 20 KO). (**B**) Time when $[Ca^{2+}]_m$ rise was at the half maxima upon PFES, calculated from the traces in panel A. (**C**) Basal $[Ca^{2+}]_m$ levels were measured in the neurons expressing mitochondrial targeted ratio metric sensor GEM-GECO; the bar graph represents the GEM-GECO-470/535 ratios ($N = 54$ WT and 53 KO). (**D**) Mean $[Ca^{2+}]_c$ traces and (**E**) maximum $[Ca^{2+}]_c$ rise induced by FCCP (2 μM) and oligomycin (10 μM) in primary cortical neurons ($N = 23$ WT and 22 KO). $P > 0.05$; $^{**}P < 0.01$; $^{***}P < 0.001$.

that loss of neurons in nKO mice might be caused by $[Ca^{2+}]_m$ overload–induced cell death. To test this possibility, we first measured the initial $[Ca^{2+}]_c$ and $[Ca^{2+}]_m$ signals simultaneously upon excitotoxic glutamate challenge (fig. S3, E and F). The $[Ca^{2+}]_c$ signals did not differ in WT and KO neurons (fig. S3, E, G, and J to L). However, similarly to Bicu + 4AP and electrical stimulation, we found that the $[Ca^{2+}]_m$ rise initiated earlier (fig. S3, F, H, and M) and was more closely coupled to the $[Ca^{2+}]_c$ rise (fig. S3I) in the absence of MICU1.

To check whether the glutamate challenge caused delayed $[Ca^{2+}]_c$ dysregulation (DCD), we monitored $[Ca^{2+}]_c$ simultaneously with the $\Delta\Psi_m$ for longer periods of time (Fig. 5, A to G). The glutamate-induced initial $[Ca^{2+}]_c$ rise was followed by a progressive secondary phase of $[Ca^{2+}]_c$ increase and was coupled with mitochondrial depolarization in both genotypes. However, the secondary phase of the $[Ca^{2+}]_c$ rise and associated $\Delta\Psi_m$ loss were evident earlier and larger in MICU1-KO neurons (Fig. 5, E to G). Moreover, the uncoupler-induced mitochondrial depolarization caused a smaller additional $[Ca^{2+}]_c$ rise in the KO (Fig. 5, A to G). Thus, depolarized mitochondria discharge their Ca^{2+} content and fail as a Ca^{2+} buffer to serve as a source of the enhanced delayed $[Ca^{2+}]_c$ rise in the KO neurons and could confer vulnerability to the glutamate-induced DCD.

Excitotoxic glutamate induces DCD via mitochondrial Ca^{2+} overload and the ensuing PTP opening (*39*). A pharmacological evidence for the involvement of PTP opening was that preincubation with NIM811, a potent blocker of the PTP, delayed the occurrence of glutamate-induced DCD (Fig. 5H). As NIM811 blocks PTP by binding to cyclophilin, we compared the protein levels of cyclophilin D in WT and KO neurons and found no difference (fig. S2D). We next tested the glutamate-induced neuronal cell death by measuring plasma membrane permeabilization over time (Fig. 5, I and J). The rate of glutamate-induced cell death was approximately twofold higher in the KO neurons as compared with WT. We carried out similar experiments with heterozygous MICU1$^{+/-}$ (HT) neurons having one functional allele of MICU1 and found no major differences in glutamate-induced DCD between WT and heterozygous neurons (fig. S4, B to H) and neuronal viability (fig. S4, I to J). Immunoblot analysis for uniporter complexes showed no difference between HT and WT neurons (fig. S4A), suggesting that a single allele of MICU1 in HT is sufficient to produce MICU1 protein comparably to that in WT. This result also explains why HT neurons produced similar response to excitotoxic glutamate as in WT. Thus, the complete loss of MICU1 makes primary cortical neurons more vulnerable to $[Ca^{2+}]_m$ overload and PTP opening, culminating in progressive neuronal death.

To test whether the same pathway might apply to the neurons of the adult nKO mice, we evoked $[Ca^{2+}]_m$ overload in isolated cortical mitochondria by applying a series of Ca^{2+} boluses. We found that mitochondria from nKO mice tolerated fewer Ca^{2+} pulses before the precipitous $[Ca^{2+}]_c$ rise occurred (Fig. 5, K and L, and fig. S2E). We postulated that it was mediated through PTP opening, and this idea was validated pharmacologically by the protective effect of cyclosporin A (CsA), an inhibitor of the PTP (Fig. 5, K and L).

MICU1-deficent patient cells are sensitized to delayed Ca^{2+} dysregulation and cell death

Similar to the MICU1-KO neurons, human MICU1-deficient patient fibroblasts (*9*) also have lower activation threshold for mitochondrial

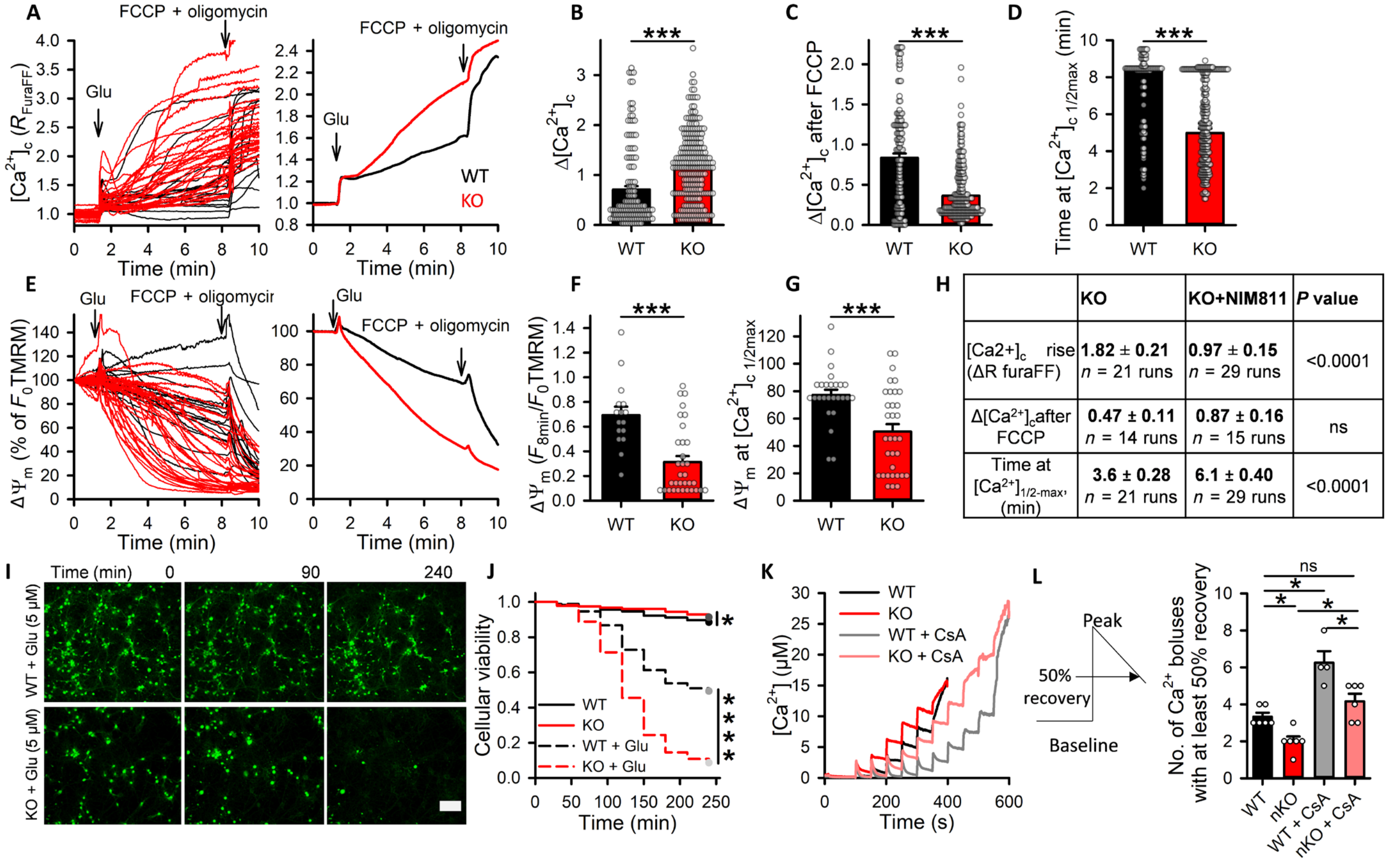

	KO	KO+NIM811	*P* value
[Ca2+]$_c$ rise (ΔR furaFF)	**1.82 ± 0.21** *n* = 21 runs	**0.97 ± 0.15** *n* = 29 runs	<0.0001
$\Delta[Ca^{2+}]_c$after FCCP	**0.47 ± 0.11** *n* = 14 runs	**0.87 ± 0.16** *n* = 15 runs	ns
Time at $[Ca^{2+}]_{1/2\text{-max}}$, (min)	**3.6 ± 0.28** *n* = 21 runs	**6.1 ± 0.40** *n* = 29 runs	<0.0001

Fig. 5. Enhanced susceptibility to glutamate-induced delayed Ca^{2+} dysregulation and cell death in MICU1-KO neurons. (**A**) Individual (left) and mean (right) $[Ca^{2+}]_c$ traces measured in primary cortical neurons upon 5 μM glutamate (Glu) stimulation by furaFF. (**B**) Baseline subtracted Glu-induced $[Ca^{2+}]_c$ rise. (**C**) Additional $[Ca^{2+}]_c$ rise upon FCCP (2 μM) and oligomycin (10 μM) addition after Glu stimulation, measured as shown in (A) by subtracting $[Ca^{2+}]_c$ of 8 min from that at 10 min. (**D**) Time to reach the half-maximal $[Ca^{2+}]_c$ rise. (**E**) $\Delta\Psi_m$ measured with TMRM simultaneously with $[Ca^{2+}]_c$ [see (A)]. Individual (left) and mean (right) traces. (**F**) Glu-induced depolarization relative to FCCP + oligomycin–induced depolarization. (**G**) $\Delta\Psi_m$ normalized to baseline at the median half-maximal time of the Glu-induced $[Ca^{2+}]_c$ rise [see (D)]. (A to G) 16 WT, 33 KO runs with $N = 104$ WT, 257 KO neurons. (**H**) Rescue of Glu-induced maximum $[Ca^{2+}]_c$ rise with NIM811 (100 μM), uncoupler-induced residual mitochondrial Ca^{2+} discharge, and time to reach half-maximal $[Ca^{2+}]_c$ rise) in KO neurons. (**I**) Cultured primary neurons loaded with calcein-AM dye, before (0), and 90 and 240 min after Glu stimulation; scale bar, 100 μm. (**J**) Viability of neurons upon excitotoxic Glu stimulation (5 μM) ($N = 3$ independent experiments). (**K**) Ca^{2+} retention capacity measured on purified cortical mitochondria, mean traces showing the extra-mitochondrial calcium measured using furaFF after repetitive addition of 5 μM $CaCl_2$ boluses in the presence or absence of cyclosporine A (5 μM, CsA added at 0 s) ($N = 3$). (**L**) Mitochondrial Ca^{2+} retention capacity calculated as the number of calcium boluses at which extramitochondrial calcium recover at least 50% from the peak. ns, not significant; $P > 0.05$; *$P < 0.05$; ***$P < 0.001$; ****$P < 0.0001$.

Ca^{2+} uptake (fig. S5, A to C) (*41*), which was rescued by reintroduction of MICU1-HA (fig. S5D). We tested here the vulnerability of MICU1-patient fibroblasts to DCD-induced cell death. We exposed the human fibroblasts to prolonged Ca^{2+} entry in combination with H_2O_2 that synergizes with Ca^{2+} in PTP opening (Fig. 6A). We observed an initial $[Ca^{2+}]_c$ peak followed by a plateau gradually turning to a second $[Ca^{2+}]_c$ increase with slow kinetics (Fig. 6A). MICU1-deficient patient cells showed higher delayed $[Ca^{2+}]_c$ increases (Fig. 6B). Cell viability was quantified by measuring the retention time of the furaFF dye in the cytoplasm along the course of the experiment. MICU1-deficient fibroblasts had higher rate of cell death compared with control cells (Fig. 6C). Reintroduction of the MICU1 gene gave protection against the secondary $[Ca^{2+}]_c$ rise (Fig. 6, D and E) and cell death (Fig. 6F) in the MICU1-deficient patient fibroblasts, confirming loss of MICU1 as the cause of DCD susceptibility. Because PTP opening is central to the DCD and the ensuing cell death, we assumed that PTP blocking by CsA would rescue patient fibroblasts from cell death. Overnight CsA (5 μM) treatment resulted in protection of patient fibroblast cells against the cell death caused by Ca^{2+} overload (Fig. 6F). The studies of the patient fibroblasts were also performed with the lymphoblasts of another MICU1-deficient patient (*15*), and the results showed the same outcome observed in the MICU1-deficient patient fibroblasts (fig. S5, E to G).

DISCUSSION

In this study, we showed that neuron-specific homozygous MICU1 deletion in mouse leads to altered neuronal Ca^{2+} homeostasis and progressive motor and cognitive dysfunction likely in both males and females. These phenotypes recapitulate those previously reported in patient fibroblasts/lymphoblasts and the symptoms displayed by many MICU1-deficient male and female patients (*12*–*15*, *62*, *63*). Heterozygous *micu1* neurons and nKO mice have no significant impairments, which is consistent with literature on most individuals with heterozygous

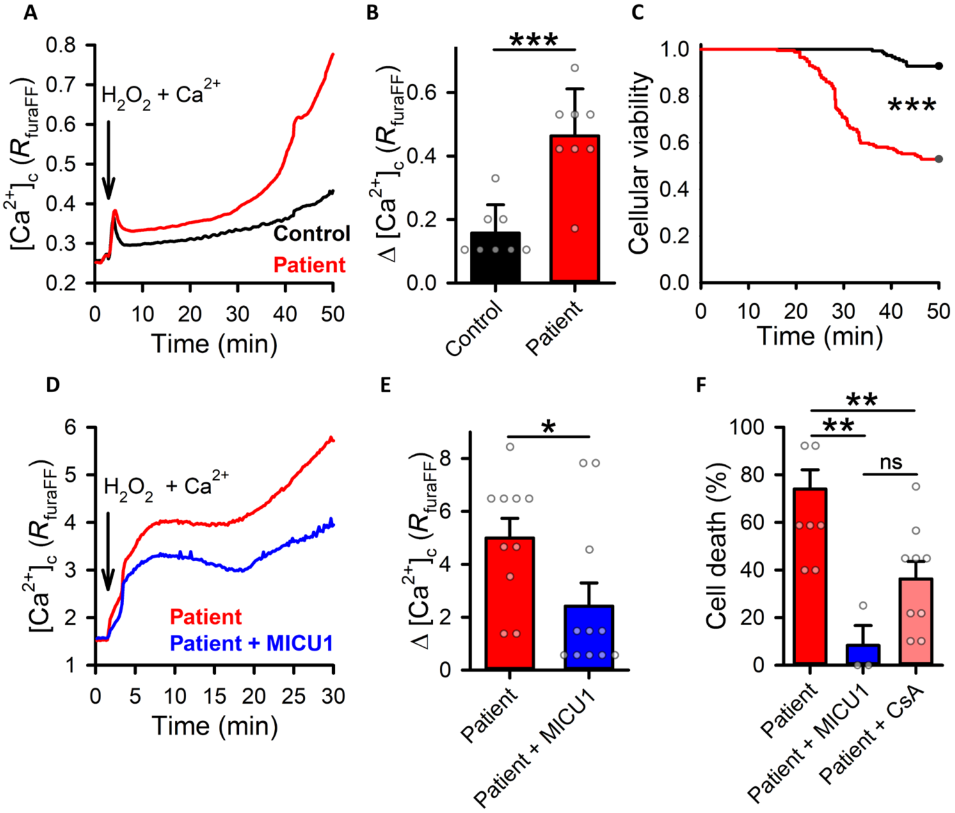

Fig. 6. Delayed Ca^{2+} dysregulation and cell death in MICU1-deficient patient fibroblasts and its prevention by MICU1 rescue. (**A**) Mean $[Ca^{2+}]_c$ traces of store-depleted human control and MICU1-deficient patient fibroblasts stimulated by the addition of H_2O_2 (1 mM) and Ca^{2+} ($CaCl_2$ 10 mM), (**B**) change in maximum $[Ca^{2+}]_c$, and (**C**) cell viability (*N* = 8 pairs of runs). (**D**) $[Ca^{2+}]_c$ traces for human MICU1-deficient patient fibroblasts rescued with MICU1, (**E**) maximum $[Ca^{2+}]_c$, and (**F**) $H_2O_2 + Ca^{2+}$–induced patient fibroblast cell death rescued with MICU1 and CsA (5 μM overnight) (*N* = 10 nonrescued, 11 MICU1 rescued, and 9 CsA rescued runs). ns, not significant; $P > 0.05$; $^{*}P < 0.05$; $^{**}P < 0.01$; $^{***}P < 0.001$.

MICU1 mutation (*14*, *15*, *62*). This is likely because lymphoblasts derived from humans with heterozygous MICU1 mutation (*15*), and neurons derived from HT mice (fig. S4) showed no decrease in the mtCU protein abundance, suggesting that one normal allele is sufficient to provide a normal amount of MICU1. Our findings that the motor defects in the nKO mouse were significant and were missing in the skeletal muscle-specific MICU1-KO mouse indicate that the pathological changes due to neuron-specific loss of MICU1 are the main cause of the motor deficiency in patients. Moreover, unaltered MICU1 protein abundance in SM mitochondria and normal muscle fiber morphology of nKO animals suggest that demise in motor function was not because SM alterations. On the basis of the nKO mouse results, it is likely that loss of MICU1 postnatally is not too late to induce neuronal pathology.

The altered structure of the dendritic spine is a hallmark of aging and neurodegeneration associated with cognitive and motor impairments (*64*–*66*). More specifically, a decrease in spine density [~20 to 30% (*65*, *67*, *68*)], length (*68*), and spine head diameter [~10 to 15% (*67*, *68*)] are found in mouse models of various neurodegenerative diseases with motor dysfunction like Parkinson's disease, Huntington's disease, and spinal cord injury. Similar structural changes are found in Alzheimer's disease mouse models and are believed to define the cognitive impairment (*69*, *70*). Consistent with these reports, we found a change in dendritic spine morphology of similar magnitude in the motor cortex of aged nKO animals (18 months), and more subtle alterations even in early age (3 months). We also found motor neuron degeneration, a hallmark in motor neuron disease (*68*, *71*, *72*), in the anterior horn of the spinal cord of nKO mice. Together, our results suggest that the loss of dendritic spine morphology from the motor cortex and motor neuron degeneration in the anterior horn of spinal cord might be plausible reasons for the behavioral abnormalities of nKO animals.

Dendritic alteration (*9*, *73*) and neurodegeneration (*6*, *7*, *74*) have been associated with altered mitochondrial Ca^{2+} homeostasis. We found the following signs of dysregulation in MICU1 neurons: (i) $[Ca^{2+}]_m$ is elevated at rest, (ii) $[Ca^{2+}]_m$ increases further from $[Ca^{2+}]_c$ elevations that are subthreshold in WT, (iii) mitochondria are prone to Ca^{2+} overload and PTP opening, and (iv) synaptic activity–related $[Ca^{2+}]_c$ signaling is altered (suppressed response to Bicu + 4AP). Moreover, we provided direct proof that altered $[Ca^{2+}]_m$ handling makes MICU1-KO neurons more vulnerable to glutamate-induced DCD and cell death, which is similar to humans in which MICU1-deficient patient-derived fibroblasts/lymphoblasts show DCD and mortality upon sustained $[Ca^{2+}]_c$ rise. These findings highlight the role of MICU1 in maintaining proper mitochondrial Ca^{2+} handling in favor of cell survival.

MICU1-KO is associated with down-regulation of EMRE and MICU3 proteins, and this raises the question whether the phenotype that we observed in the various MICU1-KO models (KO, nKO, and MICU1-deficient patient-derived fibroblasts/lymphoblasts) might have resulted from the decreased abundance of these proteins. However, in contrast to MICU1 loss, EMRE loss is known to reduce/block the mitochondrial Ca^{2+} uptake, and lowering EMRE expression protects MICU1-KO mitochondria against Ca^{2+} overload and ameliorates MICU1-KO phenotype in mice (*26*, *46*). Thus, EMRE down-regulation seems to be part of an adaptive action to decrease mitochondrial Ca^{2+} uptake. Nevertheless, the compensation by EMRE loss is insufficient to prevent Ca^{2+} overload. MICU3 was described to positively regulate mtCU function through the formation of dimers with MICU1 and to interact with mtCU only as a MICU1-MICU3 heterodimer (*33*). The MICU3 protein decrease in the absence of MICU1 might occur because the monomeric MICU3 becomes unstable and gets degraded or because a feedback mechanism inhibits its expression either at the transcriptional or translational level. Because MICU3 cannot bind to the mtCU in the absence of MICU1, MICU3 is unlikely to have its own role in the MICU1-KO phenotype.

Mitochondrial Ca^{2+} uptake is critical for glutamate-induced DCD (*75*). Therefore, we predict that pharmacological targeting of the mtCU could alleviate DCD and neuronal injury. Likewise, the protective effect of PTP inhibitors in both neurons and patient fibroblasts points to another potential therapeutic strategy. In summary, our results identify a progressive chain of events starting from altered neuronal mitochondrial Ca^{2+} uptake and Ca^{2+} overload that leads to abnormal dendritic spine barbarization and neuronal death that culminates in the development of motor and cognitive disabilities seen in human MICU1 patients. These results are also expected to stimulate studies of a possible role of MICU1 in determining the pathophysiology in common neurological disorders.

MATERIALS AND METHODS

Generation of the MICU1-KO/KO mice

All animals were used in accordance with the mandated standards of humane care and were approved by the Thomas Jefferson University Institutional Animal Care and Use Committee. To obtain MICU1 floxed ($MICU1^{F/F}$) and MICU1-KO ($MICU1^{-/-}$) mice, the Cre-loxP system was used to target exon 3 of the MICU1 gene for removal on C57BL/6J background as described earlier (*42*).

Generation of the neuron-specific MICU1 knockdown mice

To obtain neuron-specific MICU1-KO mice MICU1-nKO, $Eno2^{cre}$ mice (the Jackson Laboratory) were crossed with the $MICU1^{F/F}$ mice. Genotypes were determined by polymerase chain reaction (PCR) analysis of genomic DNA isolated from tail biopsies using the following primers: loading control—CAGE NDEL, **5**′-GGTGGAGTCAAAGGGAGGAACAG-3′ (forward) and 5′GCCCCATCTATGATAATGTTAAGC-3′ (reverse); MICU1 deletion—KO, 5′-ATGAGCATGAAGTGATGACCCGAC-3′ (forward) and 5′-GCCCCATCTATGATAATGTTAAGC-3′ (reverse); Cre expression—Cre, 5′-CAGAACCTGAAGATGTTCGC-3′ (forward) and 5′-TACACCTCGGTGCTAACCAG-3′ (reverse). smKO animals were bred as described earlier (*41*).

Tissue isolation and histological analysis

Male and female mice of different age groups were euthanized by cervical dislocation.

Tibialis anterior muscle from 9-month-old animals were isolated, fixed in 10% neutral buffered formalin, and then embedded in paraffin. Hematoxylin and eosin staining was performed at the translational research/pathology shared resource at the Thomas Jefferson University. Images were acquired using a Zeiss Axio Observer microscope with DFC420 digital camera (Leica). Muscle fiber area, perimeter, Feret, and minimum Feret were measured in ImageJ [National Institutes Health (NIH)].

Brain and spinal cord were dissected from euthanized male mice, then washed with 0.1 M phosphate-buffered saline (PBS), and then fixed in ice-cold 4% paraformaldehyde for 48 hours and subsequently cryopreserved in 30% sucrose for 48 hours. Coronal sections of 10 μm were cut using cryotome, mounted on gelatin-coated glass slides, and dried overnight at room temperature. Nissl (cresyl violet) staining was performed as described earlier (*76*). For Golgi staining, the brain tissue was processed following the manufacturer's protocol (FD Rapid GolgiStain Kit, no. PK401A).

For immunostaining, the sections were washed with 0.1 M PBS (three times), permeabilized with 0.4% Triton X-100, blocked with 5% normal goat serum, and incubated with the primary antibody overnight at 4°C (ChAT, ab178850, 1:250 and GFAP, ab7260, 1:1000). The sections were washed twice with PBS and followed by incubation with fluorescence-tagged (Alexa Fluor 488) secondary antibodies (1:250) for 24 hours. Immunostained sections were washed twice with PBS and mounted with Antifade, photographed using a Zeiss LSM 880 confocal microscope, and analyzed in ImageJ (NIH).

Isolation of mitochondria

Mitochondria from cerebral cortex of male and female mice were isolated using Percoll (Sigma-Aldrich, St. Louis, MO) density gradient as described previously (*77*, *78*).

Protein extracts and Western blotting

Protein lysates from tissues or mitochondria were prepared in radioimmunoprecipitation assay (RIPA) buffer (Sigma-Aldrich) supplemented with protease inhibitors [leupetin, antipain, pepstatin, and phenylmethylsulfonyl fluoride (PMSF); Sigma-Aldrich]. Equivalent amounts of total protein (50 μg) were separated electrophoretically by SDS–polyacrylamide gel electrophoresis (10 or 12% TGX gels, Bio-Rad) in reducing conditions, transferred to a nitrocellulose membrane (Bio-Rad) then blocked in Odyssey blocking solution (LI-COR) for 1 hour at room temperature, and probed overnight at 4°C using the following primary antibodies: MICU1 (Sigma-Aldrich, HPA037480; 1:500), MICU2 (Abcam, ab101465; 1:500), MCU (Sigma-Aldrich, HPA016480; 1:500), MICU3 (Sigma-Aldrich, HPA024048; 1:1000), EMRE (Santa Cruz Biotechnology, sc-86337; 1:200), anti-CCDC109B/MCUB (Abcam, ab170715; 1:1000), NCLX (Santa Cruz, sc161921; 1:500), cyclophilin D (Abcam, ab110324; 1:1000), and Hsp70 (Thermo Fisher Scientific, MA3-028; 1:1000). Membranes were scanned using an Odyssey scanner (LI-COR) after incubation with fluorescent secondary antibodies. Quantification was performed using ImageJ (NIH) (*36*).

RNA isolation and quantitative PCR

Total RNA were extracted from cells using the Animal Tissue RNA Purification Kit (Norgen) according to the manufacturer's instructions. Quantification was done on the nanophotometer Pearl (Implen). cDNA was synthesized using SuperScript III (Invitrogen) and used for quantitative PCRs (qPCRs) using SYBR Green (Invitrogen) on an ABI Prism 7000 sequence detection system (Life Technologies). Data were analyzed using the comparative 2−ΔΔCt method. Ct of the gene of interest was normalized to that of β-actin. Primers used are listed as follows: MICU1, 5′-AACAGCAAGAAGCCTGACAC-3′ (forward) and 5′-CTCATTGGGCGTTATGGAG-3′ (reverse); MICU2, 5′-GGAGCGTAAAACACTGGTC-3′ (forward) and 5′-GTAAGCAAGAAAAGATACTCGG-3′ (reverse); MICU3, 5′-GCCCAAATTTGCTAAAACGTG-3′ (forward) and 5′-TCTAAAACCTGCATGGGGCT-3′ (reverse); EMRE, 5′-TCAGTCATCGTCACTCGC-3′ (forward) and 5′-AAGCAGAGCAGCGAAGTTC-3′ (reverse); MCU, 5′-TACTCACCAGATGGCGTTC-3′ (forward) and 5′-GTCCTCTAACCTCTCCAC-3′ (reverse); β-actin, 5′-CAACACCCCAGCCATG-3′ (forward) and 5′-GTCACGCACGATTTCCC-3′ (reverse).

Behavioral tests

Behavioral tests were performed on male and female mice in different age groups.

Grip test

Grip test was performed to analyze their limb strength. Animals were allowed to grasp a 4-mm-diameter metal bar placed horizontally about 50-cm height from a soft bedding with their fore paw. Latency of animal to fall from the bar was recorded for five trials with 1 to 2 min of recovery period after each trial, and the scores were averaged. Animals were removed from the bar when the criterion time of 60 s was reached (*79*).

Rotarod

Sensorimotor coordination and balance were assessed using Rotamex 4/5 device (Columbus Instruments, Columbus, OH). Animals were tested for 3 days, three trials each day, on a rotating rod accelerating gradually from 12 to 35 rpm in 3 min. Latencies for the mouse to fall from the rod were recorded (*48*).

Pole test

Vertical pole task was done using a 55-cm-long and 0.8-cm-diameter wooden pole. Animals were placed on the top part of the pole head facing upward. Latencies to turn through the 180°, to descend once turned, and to complete the task were measured for a maximum time of 120 s. Failure to turn, falling, or slipping down backward was scored with 120 s (*80*).

Barnes maze

Spatial learning and memory were tested on a brightly lit, exposed circular (1.2 m in diameter) open platform surface with a small dark recessed escape box located under 1 of the 18 evenly spaced holes around the perimeter of the platform. The position of the escape box relative to the other holes and the testing room remains fixed during the whole study.

Animals were tested for four consecutive days, four trials each day. Animals were placed under a start box in the center of the maze for 30 s, then the box was removed, and the mouse was allowed to explore freely to find the escape box for a maximum time of 150 s (*81*). Animals were video-tracked, and parameters were analyzed in ANY-maze (Stoelting Co., Wood Dale, IL).

Cortical neuronal culture

Primary embryonic neuron cultures were prepared as described earlier (*44*, *82*). Briefly, embryonic mice were removed on gestational days 14 to 16, and the brains were removed. Cortical hemispheres were dissected, chopped, and incubated for 10 min in Dulbecco's modified Eagle's medium (DMEM; Sigma-Aldrich, St. Louis, MO) containing 0.25% trypsin. The digestion reaction was then stopped by adding DMEM supplemented with 10% fetal bovine serum (FBS) and spun for 2 min at 200*g*. The pellet was further washed two times with DMEM with FBS. Supernatant was discarded, and the brains were triturated 10 to 14 times in neurobasal medium without supplement and spun down for 5 min at 200*g*. The pellet was resuspended in neurobasal medium with B27 (Gibco, 17504-044) and GlutaMAX (Thermo Fisher Scientific, 35050-061). After trituration, cells were passed through a 75-μm strainer and plated on 25-mm coverslips (Carolina Biological Supply Co., Burlington, NC) coated with poly(L-lysine) (Sigma-Aldrich, P1524) and maintained in a humidified incubator at 37°C in 5% CO_2.

Human fibroblast culture

Human fibroblast cells (*13*) were created and gifted by R. Horvath (Newcastle). Cells were grown in DMEM medium supplemented with 10% FBS (Gibco), penicillin (100 U/ml), streptomycin (100 μg/ml), and 2 mM glutamine (Gibco) and kept in 37°C and 5% CO_2.

Human lymphoblast culture

Human lymphoblasts (*15*) were created and gifted by A. Roos (Essen). Cells were cultured at 37°C in a 5% CO_2 atmosphere. RPMI 1640 medium with L-glutamine (Gibco) with 20% FBS (Gibco), 1% penicillin/streptomycin was used.

Transfection

Primary cortical neurons or human fibroblasts were transfected with Lipofectamine 3000 (Invitrogen) according to the manufacturer's instructions using the following constructs: mtRCaMP, mtGCaMP6f, mtGem-GECO1, MICU1-HA, and mito-Cepia. To rescue the human MICU1-deficient patient fibroblasts with MICU1, the MICU1-HA and the fluorescent, mitochondrial targeted mito-Cepia constructs were cotransfected in a 1:1 ratio. Transfected cells were identified under a fluorescence microscope.

Ca^{2+} imaging experiments

Primary cortical neurons or human fibroblasts were plated on 25-mm glass coverslips. Fibroblast cells were transfected 48 hours before imaging experiments, and primary neurons were transfected at day 7 after culture and imaged between 13 and 15 days after plating. For measurements of $[Ca^{2+}]_{cyto}$, neurons were loaded with 2 μM fura2/acetoxymethyl ester (AM) (Invitrogen) or furaFF/AM (Invitrogen) in Hanks' balanced salt solution (HBSS; Gibco, 14025076) in the presence of 0.003% Pluronic F-127 for 30 min at 37°C.

Fibroblasts were loaded with 2 μM fura2/AM (Invitrogen) or furaFF/AM (Invitrogen) in serum-free extracellular medium [ECM; 121 mM NaCl, 5 mM $NaHCO_3$, 10 mM Na-Hepes, 4.7 mM KCl, 1.2 mM KH_2PO_4, 1.2 mM $MgSO_4$, 2 mM $CaCl_2$, and 10 mM glucose (pH 7.4)] containing 2% bovine serum albumin (BSA) (Roche) in the presence of 0.003% Pluronic F-127 and 100 μM sulfinpyrazone for 10 min at 37°C. For store-operated Ca^{2+} entry, fibroblast cells were predepleted with 2 μM thapsigargin (Enzo), and global $[Ca^{2+}]_c$ were raised by adding back 10 mM $CaCl_2$ in the presence or absence of 1 mM H_2O_2 in Ca^{2+}-free ECM containing 0.25% BSA.

For $[Ca^{2+}]_c$ and $[Ca^{2+}]_m$ imaging, we used a ProEM1024 EMCCD camera (Princeton Instruments) fitted to a Leica DMI6000B inverted microscope with Lambda DG4 wavelength-switch xenon light source (Sutter Instruments), operated by a custom software

(Spectralyzer). Fura2 fluorescence was recorded at 340- and 380-nm excitation, and the mitochondrial matrix-targeted mtCEPIA and GCaMP6f was excited at 485/15 nm, RCaMP at 545/20 nm, and mtGEM-GECO at 405 nm using dual-band dichroic and emission filter (Chroma, set 73100). The images were acquired from 200-ms to 1.5-s interval. Traces for fluorescence intensities were obtained by taking average from all cells in a field and were considered as one measurement.

$[Ca^{2+}]_m$ traces obtained from nonratiometric sensors were normalized to their baseline intensity obtained before stimulation. Basal $[Ca^{2+}]_m$ was measured by calculating the ratio of blue (470 nm) and green (535 nm) emission of mtGEM-GECO. $[Ca^{2+}]_c$ measurements with fura2 in intact cells were calibrated in vitro as described (*83*).

Pulse field electric stimulation

Primary cortical neurons cultured on glass coverslip were placed on the O-ring–based perfusion chamber with stimulator (RC-49MFSH) and filled with 150 μl of imaging buffer (HBSS added with 50 μM D,L-2-amino-5-phosphonovaleric acid and 10 μM GYKI-52466-HCl; Sigma-Aldrich). During field stimulation, neurons were continuously perfused with the imaging buffer using gravity-based custom-made perfusion system. The action potentials were evoked at 40 V/cm field achieved by passing 150 pulses (2-ms pulse, 20 Hz) of current using platinum field stimulation electrode (RC-49MFSH). The $[Ca^{2+}]_c$ and $[Ca^{2+}]_m$ rise evoked by electric field stimulation was imaged as described above in calcium imaging panel.

Mitochondrial Ca^{2+} uptake study

Fluorometric measurements of mitochondrial Ca^{2+} clearance were performed as previously described (*20*). Briefly, 300 μg (for PTP experiment) and 750 μg (for uptake study) of isolated mouse brain cortical mitochondrial protein were resuspended in 1.5 ml of intracellular medium [120 mM KCl, 10 mM NaCl, 1 mM KH_2PO_4, 20 mM tris-Hepes (pH 7.2)] supplemented with proteases inhibitors (leupetin, antipain, and pepstatin, 1 μg/ml each), 2 mM Mg–adenosine 5′-triphosphate (ATP), and 2 μM thapsigargin (Enzo) and maintained in a stirred thermostated cuvette at 35°C. For PTP experiments, the intracellular medium was used without Mg-ATP. Assays were performed in the presence of 20 μM CGP-37157 (Enzo) and 1 mM malate/pyruvate using a DeltaRAM fluorimeter (Photon Technology International). The extramitochondrial Ca^{2+} concentration $[Ca^{2+}]_c$ was measured by the ratiometric Ca^{2+} probe furaFF (1 μM) using 340- to 380-nm excitation and 500-nm emission. Calibration of the furaFF signal was carried out at the end of each measurement, adding 1 mM $CaCl_2$, followed by 10 mM EGTA/tris (pH 8.5).

Measurement of $\Delta\Psi_m$

Primary neurons were loaded with 6 nM TMRM in HBSS for 30 min. Dye was excited at 545/20 nm, and, to avoid TMRM depletion while imaging, the bath solution was incubated with 3 nM TMRM.

Viability test

Human fibroblast cells were loaded with furaFF/AM and treated with thapsigargin (2 μM) in Ca^{2+}-free ECM. Ca^{2+} (10 mM) and H_2O_2 (1 mM) were added to induce delayed calcium dysregulation. furaFF signal was recorded for 50 min at 10-s time interval. For the rescue experiments, cells were cotransfected with MICU1-HA and mtGCaMP6f. To test the dependence of the phenotype on PTP opening, fibroblast cells were incubated with 5 μM CsA overnight.

Primary cortical neurons were loaded with 2 μM of calcein-AM (Invitrogen) in the presence of 0.003% Pluronic F-127 in HBSS medium. Neurons were stimulated with 5 μM glutamate and imaged for 4 hours with 30-min intervals. The number of cells were counted in each frame.

Statistical analysis

Data are expressed as means ± SEM unless stated otherwise. Box plots are shown as follows: center line, median; box limits, upper and lower quartiles; whiskers, 1.5× interquartile range; and points, outliers. Experiments were performed at least three times in duplicates or more. When comparing two groups, statistical analysis was performed using the unpaired, two-tailed Student's *t* test [Figs. 1 (B to D, F, and G), 2 (G {3 months} and I), 3 (A to C and H), 4 (B and E), 5 (B to D and F to H), and 6E; figs. S1 (B {grip test and rotarod, pole test at 3 months} to D, S2 (A to D), and S4A] or Mann-Whitney rank sum test when normality or equal variance test failed [Figs. 1H, 2 (A to C and G {18 months}), 3 (E and K), 5H, and 6B; figs. S1 (B {pole test at 9 months} and E), S3 (J to M), S4 (C to E, G, and H), and S5 (A to C and F)]. In the above cases, data are expressed as means ± SD. For multiple comparisons, we used one-way analysis of variance (ANOVA) (Figs. 5L and 6F). To compare two groups with repeated measurements, two-way ANOVA was used (Holm-Sidak method) (Figs. 1E and 2F). Survival curves were analyzed with Kaplan-Meier survival analysis with log-rank (Figs. 5J and 6C, and figs. S4J and S5G).

Statistical significance was labeled as follows: not significant (ns), $P > 0.05$; $^*P < 0.05$; $^{**}P < 0.01$; $^{***}P < 0.001$; $^{****}P < 0.0001$. All statistical tests were performed using Systat SigmaPlot 12.5.

SUPPLEMENTARY MATERIALS

Supplementary material for this article is available at https://science.org/doi/10.1126/sciadv.abj4716

View/request a protocol for this paper from *Bio-protocol*.

REFERENCES AND NOTES

1. R. Rizzuto, D. De Stefani, A. Raffaello, C. Mammucari, Mitochondria as sensors and regulators of calcium signalling. *Nat. Rev. Mol. Cell Biol.* **13**, 566–578 (2012).
2. N. Plotegher, R. Filadi, P. Pizzo, M. R. Duchen, Excitotoxicity revisited: Mitochondria on the verge of a nervous breakdown. *Trends Neurosci* **44**, 342–351 (2021).
3. M. Calvo-Rodriguez, B. J. Bacskai, Mitochondria and calcium in Alzheimer's disease: From cell signaling to neuronal cell death. *Trends Neurosci.* **44**, 136–151 (2021).
4. D. J. Surmeier, P. T. Schumacker, J. D. Guzman, E. Ilijic, B. Yang, E. Zampese, Calcium and Parkinson's disease. *Biochem. Biophys. Res. Commun.* **483**, 1013–1019 (2017).
5. P. Jadiya, J. F. Garbincius, J. W. Elrod, Reappraisal of metabolic dysfunction in neurodegeneration: Focus on mitochondrial function and calcium signaling. *Acta Neuropathol. Commun.* **9**, 124 (2021).
6. N. Plotegher, M. R. Duchen, Crosstalk between lysosomes and mitochondria in Parkinson's disease. *Front. Cell Dev. Biol.* **5**, 110 (2017).
7. A. Grimm, A. Eckert, Brain aging and neurodegeneration: From a mitochondrial point of view. *J. Neurochem.* **143**, 418–431 (2017).
8. M. J. Devine, J. T. Kittler, Mitochondria at the neuronal presynapse in health and disease. *Nat. Rev. Neurosci.* **19**, 63–80 (2018).
9. M. Verma, Z. Wills, C. T. Chu, Excitatory dendritic mitochondrial calcium toxicity: Implications for Parkinson's and other neurodegenerative diseases. *Front. Neurosci.* **12**, 523 (2018).
10. J. M. Oliveira, S. Chen, S. Almeida, R. Riley, J. Gonçalves, C. R. Oliveira, M. R. Hayden, D. G. Nicholls, L. M. Ellerby, A. C. Rego, Mitochondrial-dependent Ca2+ handling in Huntington's disease striatal cells: Effect of histone deacetylase inhibitors. *J. Neurosci.* **26**, 11174–11186 (2006).
11. A. H. Schapira, C. W. Olanow, J. T. Greenamyre, E. Bezard, Slowing of neurodegeneration in Parkinson's disease and Huntington's disease: Future therapeutic perspectives. *Lancet* **384**, 545–555 (2014).
12. C. V. Logan, G. Szabadkai, J. A. Sharpe, D. A. Parry, S. Torelli, A.-M. Childs, M. Kriek, R. Phadke, C. A. Johnson, N. Y. Roberts, D. T. Bonthron, K. A. Pysden, T. Whyte,

I. Munteanu, A. R. Foley, G. Wheway, K. Szymanska, S. Natarajan, Z. A. Abdelhamed, J. E. Morgan, H. Roper, G. W. E. Santen, E. H. Niks, W. L. van der Pol, D. Lindhout, A. Raffaello, D. De Stefani, J. T. den Dunnen, Y. Sun, I. Ginjaar, C. A. Sewry, M. Hurles, R. Rizzuto; UK10K Consortium, M. R. Duchen, F. Muntoni, E. Sheridan, Loss-of-function mutations in MICU1 cause a brain and muscle disorder linked to primary alterations in mitochondrial calcium signaling. *Nat. Genet.* **46**, 188–193 (2014).

13. D. Lewis-Smith, K. J. Kamer, H. Griffin, A. M. Childs, K. Pysden, D. Titov, J. Duff, A. Pyle, R. W. Taylor, P. Yu-Wai-Man, V. Ramesh, R. Horvath, V. K. Mootha, P. F. Chinnery, Homozygous deletion in MICU1 presenting with fatigue and lethargy in childhood. *Neurol. Genet.* **2**, e59 (2016).
14. S. Musa, W. Eyaid, K. Kamer, R. Ali, M. al-Mureikhi, N. Shahbeck, F. al Mesaifri, N. Makhseed, Z. Mohamed, W. AlShehhi, V. K. Mootha, J. Juusola, T. Ben-Omran, A Middle Eastern founder mutation expands the genotypic and phenotypic spectrum of mitochondrial MICU1 deficiency: A report of 13 patients. *JIMD Rep.* **43**, 79–83 (2019).
15. N. Kohlschmidt, M. Elbracht, A. Czech, M. Häusler, V. Phan, A. Töpf, K. T. Huang, A. Bartok, K. Eggermann, S. Zippel, T. Eggermann, E. Freier, C. Groß, H. Lochmüller, R. Horvath, G. Hajnóczky, J. Weis, A. Roos, Molecular pathophysiology of human MICU1-deficiency. *Neuropathol. Appl. Neurobiol.* **47**, 840–855 (2021).
16. K. M. Wilton, J. A. Morales-Rosado, D. Selcen, K. Muthusamy, S. Ewing, K. Agre, K. Nickels, E. W. Klee, M. L. Ho, E. Morava, Developmental brain abnormalities and acute encephalopathy in a patient with myopathy with extrapyramidal signs secondary to pathogenic variants in MICU1. *JIMD Rep.* **53**, 22–28 (2020).
17. K. J. Kamer, V. K. Mootha, The molecular era of the mitochondrial calcium uniporter. *Nat. Rev. Mol. Cell Biol.* **16**, 545–553 (2015).
18. D. De Stefani, R. Rizzuto, T. Pozzan, Enjoy the trip: Calcium in mitochondria back and forth. *Annu. Rev. Biochem.* **85**, 161–192 (2016).
19. Y. Kirichok, G. Krapivinsky, D. E. Clapham, The mitochondrial calcium uniporter is a highly selective ion channel. *Nature* **427**, 360–364 (2004).
20. G. Csordas, T. Golenár, E. L. Seifert, K. J. Kamer, Y. Sancak, F. Perocchi, C. Moffat, D. Weaver, S. de la Fuente Perez, R. Bogorad, V. Koteliansky, J. Adijanto, V. K. Mootha, G. Hajnóczky, MICU1 controls both the threshold and cooperative activation of the mitochondrial Ca^{2+} uniporter. *Cell Metab.* **17**, 976–987 (2013).
21. B. A. Simms, G. W. Zamponi, Neuronal voltage-gated calcium channels: Structure, function, and dysfunction. *Neuron* **82**, 24–45 (2014).
22. D. Lim, G. Dematteis, L. Tapella, A. A. Genazzani, T. Calì, M. Brini, A. Verkhratsky, Ca^{2+} handling at the mitochondria-ER contact sites in neurodegeneration. *Cell Calcium* **98**, 102453 (2021).
23. R. Bagur, G. Hajnoczky, Intracellular Ca^{2+} Sensing: Its role in calcium homeostasis and signaling. *Mol. Cell* **66**, 780–788 (2017).
24. D. De Stefani, A. Raffaello, E. Teardo, I. Szabo, R. Rizzuto, A forty-kilodalton protein of the inner membrane is the mitochondrial calcium uniporter. *Nature* **476**, 336–340 (2011).
25. J. M. Baughman, F. Perocchi, H. S. Girgis, M. Plovanich, C. A. Belcher-Timme, Y. Sancak, X. R. Bao, L. Strittmatter, O. Goldberger, R. L. Bogorad, V. Koteliansky, V. K. Mootha, Integrative genomics identifies MCU as an essential component of the mitochondrial calcium uniporter. *Nature* **476**, 341–345 (2011).
26. Y. Sancak, A. L. Markhard, T. Kitami, E. Kovács-Bogdán, K. J. Kamer, N. D. Udeshi, S. A. Carr, D. Chaudhuri, D. E. Clapham, A. A. Li, S. E. Calvo, O. Goldberger, V. K. Mootha, EMRE is an essential component of the mitochondrial calcium uniporter complex. *Science* **342**, 1379–1382 (2013).
27. F. Perocchi, V. M. Gohil, H. S. Girgis, X. R. Bao, J. E. McCombs, A. E. Palmer, V. K. Mootha, MICU1 encodes a mitochondrial EF hand protein required for Ca^{2+} uptake. *Nature* **467**, 291–296 (2010).
28. M. Plovanich, R. L. Bogorad, Y. Sancak, K. J. Kamer, L. Strittmatter, A. A. Li, H. S. Girgis, S. Kuchimanchi, J. de Groot, L. Speciner, N. Taneja, J. OShea, V. Koteliansky, V. K. Mootha, MICU2, a paralog of MICU1, resides within the mitochondrial uniporter complex to regulate calcium handling. *PLOS ONE* **8**, e55785 (2013).
29. M. Patron, V. Granatiero, J. Espino, R. Rizzuto, D. De Stefani, MICU3 is a tissue-specific enhancer of mitochondrial calcium uptake. *Cell Death Differ.* **26**, 179–195 (2019).
30. M. F. Tsai, C. B. Phillips, M. Ranaghan, C. W. Tsai, Y. Wu, C. Williams, C. Miller, Dual functions of a small regulatory subunit in the mitochondrial calcium uniporter complex. *eLife* **5**, (2016).
31. M. Paillard, G. Csordás, K.-T. Huang, P. Várnai, S. K. Joseph, G. Hajnóczky, MICU1 interacts with the D-ring of the MCU pore to control its Ca^{2+} flux and sensitivity to Ru360. *Mol. Cell* **72**, 778–785.e3 (2018).
32. M. Fan, J. Zhang, C. W. Tsai, B. J. Orlando, M. Rodriguez, Y. Xu, M. Liao, M. F. Tsai, L. Feng, Structure and mechanism of the mitochondrial Ca^{2+} uniporter holocomplex. *Nature* **582**, 129–133 (2020).
33. M. Patron, V. Checchetto, A. Raffaello, E. Teardo, D. Vecellio Reane, M. Mantoan, V. Granatiero, I. Szabò, D. de Stefani, R. Rizzuto, MICU1 and MICU2 finely tune the mitochondrial Ca2+ uniporter by exerting opposite effects on MCU activity. *Mol. Cell* **53**, 726–737 (2014).
34. V. Hung, P. Zou, H. W. Rhee, N. D. Udeshi, V. Cracan, T. Svinkina, S. A. Carr, V. K. Mootha, A. Y. Ting, Proteomic mapping of the human mitochondrial intermembrane space in live cells via ratiometric APEX tagging. *Mol. Cell* **55**, 332–341 (2014).
35. K. J. Kamer, Z. Grabarek, V. K. Mootha, High-affinity cooperative Ca^{2+} binding by MICU1–MICU2 serves as an on-off switch for the uniporter. *EMBO Rep.* **18**, 1397–1411 (2017).
36. M. Paillard, G. Csordás, G. Szanda, T. Golenár, V. Debattisti, A. Bartok, N. Wang, C. Moffat, E. L. Seifert, A. Spät, G. Hajnóczky, Tissue-specific mitochondrial decoding of cytoplasmic Ca^{2+} signals is controlled by the stoichiometry of MICU1/2 and MCU. *Cell Rep.* **18**, 2291–2300 (2017).
37. P. Jadiya, D. W. Kolmetzky, D. Tomar, A. di Meco, A. A. Lombardi, J. P. Lambert, T. S. Luongo, M. H. Ludtmann, D. Praticò, J. W. Elrod, Impaired mitochondrial calcium efflux contributes to disease progression in models of Alzheimer's disease. *Nat. Commun.* **10**, 3885 (2019).
38. R. Palty, W. F. Silverman, M. Hershfinkel, T. Caporale, S. L. Sensi, J. Parnis, C. Nolte, D. Fishman, V. Shoshan-Barmatz, S. Herrmann, D. Khananshvili, I. Sekler, NCLX is an essential component of mitochondrial Na^{+}/Ca^{2+} exchange. *Proc. Natl. Acad. Sci. U.S.A.* **107**, 436–441 (2010).
39. C. B. Rueda, I. Llorente-Folch, J. Traba, I. Amigo, P. Gonzalez-Sanchez, L. Contreras, I. Juaristi, P. Martinez-Valero, B. Pardo, A. del Arco, J. Satrustegui, Glutamate excitotoxicity and Ca^{2+}-regulation of respiration: Role of the Ca2+ activated mitochondrial transporters (CaMCs). *Biochim. Biophys. Acta* **1857**, 1158–1166 (2016).
40. X. Pan, J. Liu, T. Nguyen, C. Liu, J. Sun, Y. Teng, M. M. Fergusson, I. I. Rovira, M. Allen, D. A. Springer, A. M. Aponte, M. Gucek, R. S. Balaban, E. Murphy, T. Finkel, The physiological role of mitochondrial calcium revealed by mice lacking the mitochondrial calcium uniporter. *Nat. Cell Biol.* **15**, 1464–1472 (2013).
41. V. Debattisti, A. Horn, R. Singh, E. L. Seifert, M. W. Hogarth, D. A. Mazala, K. T. Huang, R. Horvath, J. K. Jaiswal, G. Hajnóczky, Dysregulation of mitochondrial Ca^{2+} uptake and sarcolemma repair underlie muscle weakness and wasting in patients and mice lacking MICU1. *Cell Rep.* **29**, 1274–1286.e6 (2019).
42. A. N. Antony, M. Paillard, C. Moffat, E. Juskeviciute, J. Correnti, B. Bolon, E. Rubin, G. Csordás, E. L. Seifert, J. B. Hoek, G. Hajnóczky, MICU1 regulation of mitochondrial Ca^{2+} uptake dictates survival and tissue regeneration. *Nat. Commun.* **7**, 10955 (2016).
43. C. H. Kwon, J. Zhou, Y. Li, K. W. Kim, L. L. Hensley, S. J. Baker, L. F. Parada, Neuron-specific enolase-cre mouse line with cre activity in specific neuronal populations. *Genesis* **44**, 130–135 (2006).
44. T. T. Nguyen, S. S. Oh, D. Weaver, A. Lewandowska, D. Maxfield, M. H. Schuler, N. K. Smith, J. Macfarlane, G. Saunders, C. A. Palmer, V. Debattisti, T. Koshiba, S. Pulst, E. L. Feldman, G. Hajnoczky, J. M. Shaw, Loss of Miro1-directed mitochondrial movement results in a novel murine model for neuron disease. *Proc. Natl. Acad. Sci. U.S.A.* **111**, E3631–E3640 (2014).
45. S. Herculano-Houzel, The glia/neuron ratio: How it varies uniformly across brain structures and species and what that means for brain physiology and evolution. *Glia* **62**, 1377–1391 (2014).
46. J. C. Liu, J. Liu, K. M. Holmström, S. Menazza, R. J. Parks, M. M. Fergusson, Z. X. Yu, D. A. Springer, C. Halsey, C. Liu, E. Murphy, T. Finkel, MICU1 serves as a molecular gatekeeper to prevent in vivo mitochondrial calcium overload. *Cell Rep.* **16**, 1561–1573 (2016).
47. C. A. Barnes, Memory deficits associated with senescence: A neurophysiological and behavioral study in the rat. *J. Comp. Physiol. Psychol.* **93**, 74–104 (1979).
48. S. P. Brooks, S. B. Dunnett, Tests to assess motor phenotype in mice: A user's guide. *Nat. Rev. Neurosci.* **10**, 519–529 (2009).
49. J. Guo, W. Qiu, S. L. Y. Soh, S. Wei, G. K. Radda, W. Y. Ong, Z. P. Pang, W. Han, Motor neuron degeneration in a mouse model of seipinopathy. *Cell Death Dis.* **4**, e535 (2013).
50. P. Tripathi, N. Rodriguez-Muela, J. R. Klim, A. S. de Boer, S. Agrawal, J. Sandoe, C. S. Lopes, K. S. Ogliari, L. A. Williams, M. Shear, L. L. Rubin, K. Eggan, Q. Zhou, Reactive astrocytes promote ALS-like degeneration and intracellular protein aggregation in human motor neurons by disrupting autophagy through TGF-β1. *Stem Cell Rep.* **9**, 667–680 (2017).
51. Z. Li, K. Okamoto, Y. Hayashi, M. Sheng, The importance of dendritic mitochondria in the morphogenesis and plasticity of spines and synapses. *Cell* **119**, 873–887 (2004).
52. M. J. Fogarty, P. G. Noakes, M. C. Bellingham, Motor cortex layer V pyramidal neurons exhibit dendritic regression, spine loss, and increased synaptic excitation in the presymptomatic hSOD1(G93A) mouse model of amyotrophic lateral sclerosis. *J. Neurosci.* **35**, 643–647 (2015).
53. R. Kandimalla, M. Manczak, X. Yin, R. Wang, P. H. Reddy, Hippocampal phosphorylated tau induced cognitive decline, dendritic spine loss and mitochondrial abnormalities in a mouse model of Alzheimer's disease. *Hum. Mol. Genet.* **27**, 30–40 (2018).
54. G. Csordás, T. Golenár, E. L. Seifert, F. Perocchi, V. K. Mootha, G. Hajnózky, MICU1 serves as a Ca^{2+}-controlled gatekeeper for the mitochondrial Ca^{2+} uniporter. *Biophysical Journal* **102**, 163a–164a (2012).
55. G. E. Hardingham, F. J. Arnold, H. Bading, A calcium microdomain near NMDA receptors: On switch for ERK-dependent synapse-to-nucleus communication. *Nat. Neurosci.* **4**, 565–566 (2001).

56. Z. Lei, P. Deng, Y. Li, Z. C. Xu, Downregulation of Kv4.2 channels mediated by NR2B-containing NMDA receptors in cultured hippocampal neurons. *Neuroscience* **165**, 350–362 (2010).
57. G. E. Hardingham, Y. Fukunaga, H. Bading, Extrasynaptic NMDARs oppose synaptic NMDARs by triggering CREB shut-off and cell death pathways. *Nat. Neurosci.* **5**, 405–414 (2002).
58. A. Stavsky, O. Stoler, M. Kostic, T. Katoshevsky, E. A. Assali, I. Savic, Y. Amitai, H. Prokisch, S. Leiz, C. Daumer-Haas, I. Fleidervish, F. Perocchi, D. Gitler, I. Sekler, Aberrant activity of mitochondrial NCLX is linked to impaired synaptic transmission and is associated with mental retardation. *Commun. Biol.* **4**, 666 (2021).
59. G. Csordas, P. Varnai, T. Golenar, S. S. Sheu, G. Hajnoczky, Calcium transport across the inner mitochondrial membrane: Molecular mechanisms and pharmacology. *Mol. Cell. Endocrinol.* **353**, 109–113 (2012).
60. K. Mallilankaraman, P. Doonan, C. Cárdenas, H. C. Chandramoorthy, M. Müller, R. Miller, N. E. Hoffman, R. K. Gandhirajan, J. Molgó, M. J. Birnbaum, B. S. Rothberg, D. O. D. Mak, J. K. Foskett, M. Madesh, MICU1 is an essential gatekeeper for MCU-mediated mitochondrial Ca^{2+} uptake that regulates cell survival. *Cell* **151**, 630–644 (2012).
61. V. Granatiero, M. Pacifici, A. Raffaello, D. De Stefani, R. Rizzuto, Overexpression of mitochondrial calcium uniporter causes neuronal death. *Oxid. Med. Cell. Longev.* **2019**, 1–15 (2019).
62. F. Bitarafan, M. Khodaeian, E. Amjadi Sardehaei, F. Z. Darvishi, N. Almadani, Y. Nilipour, M. Garshasbi, Identification of a novel MICU1 nonsense variant causes myopathy with extrapyramidal signs in an Iranian consanguineous family. *Mol. Cell Pediatr.* **8**, 6 (2021).
63. M. Mojbafan, S. T. Nojehdeh, F. Rahiminejad, Y. Nilipour, S. H. Tonekaboni, S. Zeinali, Reporting a rare form of myopathy, myopathy with extrapyramidal signs, in an Iranian family using next generation sequencing: A case report. *BMC Med. Genet.* **21**, 77 (2020).
64. L. Huang, H. Zhou, K. Chen, X. Chen, G. Yang, Learning-dependent dendritic spine plasticity is reduced in the aged mouse cortex. *Front. Neural Circuits* **14**, 581435 (2020).
65. A. Naskar, T. Manivasagam, J. Chakraborty, R. Singh, B. Thomas, M. Dhanasekaran, K. P. Mohanakumar, Melatonin synergizes with low doses of L-DOPA to improve dendritic spine density in the mouse striatum in experimental Parkinsonism. *J. Pineal Res.* **55**, 304–312 (2013).
66. R. P. Murmu, W. Li, A. Holtmaat, J. Y. Li, Dendritic spine instability leads to progressive neocortical spine loss in a mouse model of Huntington's disease. *J. Neurosci.* **33**, 12997–13009 (2013).
67. N. Heck, S. Betuing, P. Vanhoutte, J. Caboche, A deconvolution method to improve automated 3D-analysis of dendritic spines: Application to a mouse model of Huntington's disease. *Brain Struct. Funct.* **217**, 421–434 (2012).
68. A. M. Tan, S. G. Waxman, Spinal cord injury, dendritic spine remodeling, and spinal memory mechanisms. *Exp. Neurol.* **235**, 142–151 (2012).
69. M. M. Dorostkar, C. Zou, L. Blazquez-Llorca, J. Herms, Analyzing dendritic spine pathology in Alzheimer's disease: Problems and opportunities. *Acta Neuropathol.* **130**, 1–19 (2015).
70. D. L. Moolman, O. V. Vitolo, J. P. Vonsattel, M. L. Shelanski, Dendrite and dendritic spine alterations in Alzheimer models. *J. Neurocytol.* **33**, 377–387 (2004).
71. E. Tiryaki, H. A. Horak, ALS and other motor neuron diseases. *Continuum* **20**, 1185–1207 (2014).
72. M. Swash, M. Leader, A. Brown, K. W. Swettenham, Focal loss of anterior horn cells in the cervical cord in motor neuron disease. *Brain* **109** (Pt. 5), 939–952 (1986).
73. M. Verma, J. Callio, P. A. Otero, I. Sekler, Z. P. Wills, C. T. Chu, Mitochondrial calcium dysregulation contributes to dendrite degeneration mediated by PD/LBD-associated LRRK2 mutants. *J. Neurosci.* **37**, 11151–11165 (2017).
74. R. J. Miller, The control of neuronal Ca^{2+} homeostasis. *Prog. Neurobiol.* **37**, 255–285 (1991).
75. A. K. Stout, H. M. Raphael, B. I. Kanterewicz, E. Klann, I. J. Reynolds, Glutamate-induced neuron death requires mitochondrial calcium uptake. *Nat. Neurosci.* **1**, 366–373 (1998).
76. M. B. Elliott, M. L. Oshinsky, P. S. Amenta, O. O. Awe, J. I. Jallo, Nociceptive neuropeptide increases and periorbital allodynia in a model of traumatic brain injury. *Headache* **52**, 966–984 (2012).
77. T. Kristian, Isolation of mitochondria from the CNS. *Curr. Protoc. Neurosci.* **Chapter 7**, Unit 7.22 (2010).
78. N. R. Sims, M. F. Anderson, Isolation of mitochondria from rat brain using Percoll density gradient centrifugation. *Nat. Protoc.* **3**, 1228–1239 (2008).
79. O. M. Dorchies, J. Reutenauer-Patte, E. Dahmane, H. M. Ismail, O. Petermann, O. Patthey-Vuadens, S. A. Comyn, E. Gayi, T. Piacenza, R. J. Handa, L. A. Décosterd, U. T. Ruegg, The anticancer drug tamoxifen counteracts the pathology in a mouse model of duchenne muscular dystrophy. *Am. J. Pathol.* **182**, 485–504 (2013).
80. K. Matsuura, H. Kabuto, H. Makino, N. Ogawa, Pole test is a useful method for evaluating the mouse movement disorder caused by striatal dopamine depletion. *J. Neurosci. Methods* **73**, 45–48 (1997).
81. S. S. Patil, B. Sunyer, H. Hoger, G. Lubec, Evaluation of spatial memory of C57BL/6J and CD1 mice in the Barnes maze, the multiple T-maze and in the Morris water maze. *Behav. Brain Res.* **198**, 58–68 (2009).
82. J. F. Otto, M. M. Kimball, K. S. Wilcox, Effects of the anticonvulsant retigabine on cultured cortical neurons: Changes in electroresponsive properties and synaptic transmission. *Mol. Pharmacol.* **61**, 921–927 (2002).
83. G. Csordas, C. Renken, P. Várnai, L. Walter, D. Weaver, K. F. Buttle, T. Balla, C. A. Mannella, G. Hajnóczky, Structural and functional features and significance of the physical linkage between ER and mitochondria. *J. Cell Biol.* **174**, 915–921 (2006).

Acknowledgments: We thank R. Horvath and A. Roos for providing MICU1 patient cells and J. H. Santos for comments on the manuscript. **Funding:** G.H. was supported by the National Institutes of Health grants RO1-GM102724 and RO1-HL142271. A.B. was supported by Hungarian State Eotvos Fellowship MÁEÖ2016_24 from the Tempus Public Foundation (Hungary) and a János Bolyai Research Scholarship of the Hungarian Academy of Sciences (BO/00103/20/8). M.P. was a recipient of postdoctoral fellowships from La Fondation pour la Recherche Médicale (FRM) and a grant "Aide à la mobilité" from the Institut Servier (France).

Author contributions: Conceptualization: G.H., A.B., and R.S. Investigation: R.S., A.B., M.P., A.T., and M.E. Writing original draft: G.H., A.B., R.S., and M.P. Writing—review and editing: G.H., A.B., R.S., M.E., and M.P. **Competing interests:** The authors declare that they have no competing interests. **Data and materials availability:** All data needed to evaluate the conclusions in the paper are present in the paper and/or the Supplementary Materials.

Submitted 14 May 2021
Accepted 26 January 2022
Published 18 March 2022
10.1126/sciadv.abj4716